Preprints.org

Article

Not peer-reviewed version

Microstructure and Mechanical Properties of Al-Li Alloys with Different Li Contents Prepared by Selective Laser Melting

Shuobing Shao , Zhuoheng Liang , Peng Yin , Xingyuan Li , Yongzhong Zhang *

Posted Date: 29 December 2023

doi: 10.20944/preprints202312.2226.v1

Keywords: selective laser melting; Al-Cu-Li-Mg-Ag-Sc-Zr alloys; heterostructure; tensile mechanical properties

Preprints.org is a free multidiscipline platform providing preprint service that is dedicated to making early versions of research outputs permanently available and citable. Preprints posted at Preprints.org appear in Web of Science, Crossref, Google Scholar, Scilit, Europe PMC.

Copyright: This is an open access article distributed under the Creative Commons Attribution License which permits unrestricted use, distribution, and reproduction in any medium, provided the original work is properly cited.

Preprints (www.preprints.org) | NOT PEER-REVIEWED | Posted: 29 December 2023 doi:10.20944/preprints202312.2226.v1

Disclaimer/Publisher's Note: The statements, opinions, and data contained in all publications are solely those of the individual author(s) and contributor(s) and not of MDPI and/or the editor(s). MDPI and/or the editor(s) disclaim responsibility for any injury to people or property resulting from any ideas, methods, instructions, or products referred to in the content.

Article

Microstructure and Mechanical Properties of Al-Li Alloys with Different Li Contents Prepared by Selective Laser melting

Shuobing Shao [1,2,3], Zhuoheng Liang [1,2,3], Peng Yin [1,2,3], Xinyuan Li [1,2,3] and Yongzhong Zhang [1,2,3,*]

[1] GRINM Group Corporation Limited, National Engineering & Technology Research Center for Non-Ferrous Metals Composites, Beijing 101407, China
[2] GRINM Metal Composites Technology Co., Ltd., Beijing 101407, China
[3] General Research Institute for Nonferrous Metals, Beijing 100088, China
* Correspondence: yyzhang@grinm.com; Tel.: +86-13501008631

Abstract: Research on the development of new lightweight Al-Li alloys using selective laser melting process has great potential for industrial applications. This paper reports on the development of novel aluminum-lithium alloys using selective laser melting technology. Al-Cu-Li-Mg-Ag-Sc-Zr pre-alloyed powders with lithium contents of 1 wt.%, 2 wt.% and 3 wt.%, respectively, were prepared by inert gas atomization. After SLM process optimization, the microstructure and mechanical properties of the as-formed specimens were investigated. The densification of the three newly developed alloys are 99.51 %, 98.96 % and 92.01 %, respectively. They all have good formability, with the lithium loss rate about 15 %. The as-formed alloy with 1% Li content presents good comprehensive properties with a yield strength of 412.6 ± 16.0 MPa, an ultimate tensile strength of 461.1 ± 11.7 MPa, and an elongation of 13.6 ± 1.1%. The three alloys exhibit a layered molten pool stacking morphology and have a typical heterostructure. The columnar crystals and equiaxed fine grains are alternately arranged, and most of the precipitated phases are enriched at the grain boundaries. The change of Li content mainly affects the precipitation of Cu-containing phase. When the Li content is 1 wt.%, there are θ phase, T_1 phase and T_B phase. When Li increased to 2 wt.%, T_1 and T_2 phases precipitated together. When Li reaches 3 wt.%, δ′ phase precipitates with T_2 phase. This study provides useful guidance for the future SLM forming of new crack-free and high-strength Al-Li alloys.

Keywords: selective laser melting; Al-Cu-Li-Mg-Ag-Sc-Zr alloys; heterostructure; tensile mechanical properties

1. Introduction

The pursuit of lightweighting in the aerospace field is an eternal goal. Aluminum-lithium alloys are gradually replacing traditional aluminum alloys in aerospace applications due to their low density, good corrosion resistance, high strength and toughness[1,2]. Selective Laser Melting (SLM) has the characteristics of high forming precision and is not limited by the shape of the parts, which is especially suitable for rapid forming of complex precision parts and provides an effective way to prepare lightweight structures. Therefore, the rapid fabrication of monolithic components of aluminum-lithium alloys by SLM at a lower cost meets the development needs of the aerospace field[3–5].

The most widely studied aluminum alloys in SLM are Al-Si cast aluminum alloys, of which AlSi10Mg has received the most attention. These Al-Si casting aluminum alloys have good SLM process properties due to their narrow solidification range and low shrinkage[6,7]. For commonly used deformed aluminum alloys, such as 2xxx, 5xxx, 6xxx and 7xxx series alloys, attempts to use these alloys for SLM usually result in thermal cracking[8–11]. Conventional alloys designed for casting and deformation processes are unable to take full advantage of the potential benefits of SLM's high solidification rates. As a result, the focus of research on SLM aluminum alloys has gradually shifted from cast and deformed aluminum alloys to the development of new aluminum alloy systems that can be adapted to the unique thermo-mechanical conditions of the SLM process. The first

© 2023 by the author(s). Distributed under a Creative Commons CC BY license.

Preprints (www.preprints.org) | NOT PEER-REVIEWED | Posted: 29 December 2023 doi:10.20944/preprints202312.2226.v1

commercial aluminum alloy specifically designed for SLM may be the Scalmalloy alloy(Al-4.60Mg-0.66Sc-0.42Zr-0.49Mn, wt.%)[12]. SLM formed Scalmalloy alloys are characterized by fine grain size and high tensile properties[13,14]. The results of SLM processing of commercial alloys point to the importance of grain refinement in solving the cracking problem. It is noteworthy that the content of pregnant elements such as Sc and Zr is much higher than that of conventional cast and deformed aluminum alloys[15–18].

The main challenge in developing alloys for SLM is the preparation of pre-alloyed powders with different compositions. The first approach is to mix existing deformed aluminum alloy powders with pregnant powders, and the composition of the mixed powders can be easily adjusted by controlling the amount of inoculated powders[19,20]. However, it may lead to uneven melting of the mixed powder. The second method is to use the ingot to prepare the pre-alloyed powder. The advantage is that the modified elements or in situ enhanced particles can be uniformly distributed in the powder[21,22]. Therefore, the second method is chosen for this topic.

There are fewer research reports on the SLM of Al-Li alloys. Al-Li alloys are susceptible to thermal cracking during laser processing due to the large solidification range, high coefficient of thermal expansion, and easy formation of low-melting-point eutectic grains during the solidification process[23,24]. The addition of Li elements to Al-Li alloys reduces the density of the alloys but also increases the solidification temperature range of the alloys and causes precipitation of low-melting-point eutectic grains in the intergranular zone, which results in high thermal cracking susceptibility and the tendency of thermal cracking further increases under the action of the high-energy laser beam[25–28]. The difficulty in forming Al-Li alloys by SLM processing can be solved by adding Sc and Zr elements, which is mainly attributed to the minimal lattice mismatch between the primary Al_3(Sc, Zr) precipitates and the aluminum alloy matrix, and the resulting low interfacial energy ensures an effective heterogeneous nucleation point for grain crystallization[29]. The addition of Sc/Zr elements facilitates the formation of fine equiaxed grains, which can effectively adapt to the strains generated during the SLM process and avoid solidification cracks. The primary Al_3(Sc, Zr) generated at high cooling speed can significantly increase the proportion of equiaxial grains and refine the grain. It has been shown that thermal cracks can be eliminated with suitable amount of Sc and Zr addition, and their grain refinement effect can also make the material both strong and tough[30,31].

In this study, three Al-Cu-Li-Mg-Ag-Sc-Zr alloys were designed based on the commercially 2195 Al-Li alloy. The lithium content was set at 1%, 2% and 3% to reduce the density of the alloys, and the Sc and Zr elements were added to avoid cracks. The focus is on the forming quality, microstructure and mechanical properties of the three SLM formed alloys.

2. Materials and Methods

2.1. Powder Preparation

In this experiment, the raw material Al-Cu-Li-Mg-Ag-Sc-Zr powders were prepared by inert gas atomization, and the powder size distribution and morphology of the three alloys are shown in Figure 1. The design composition is shown in Table 1. Powder size is 15-70 μm and the alloy powder is spherical with few satellites. The alloying elements were determined by gas pulsed infrared method (QB-QT-36-2014) and inductively coupled plasma atomic emission spectrometry (ICP-AES, Burbach, North Rhine-Westphalia, Germany). For the convenience of the subsequent description, the SLM formed specimens are named 1#, 2# and 3# alloys according to the level of Li content.

Preprints (www.preprints.org) | NOT PEER-REVIEWED | Posted: 29 December 2023 doi:10.20944/preprints202312.2226.v1

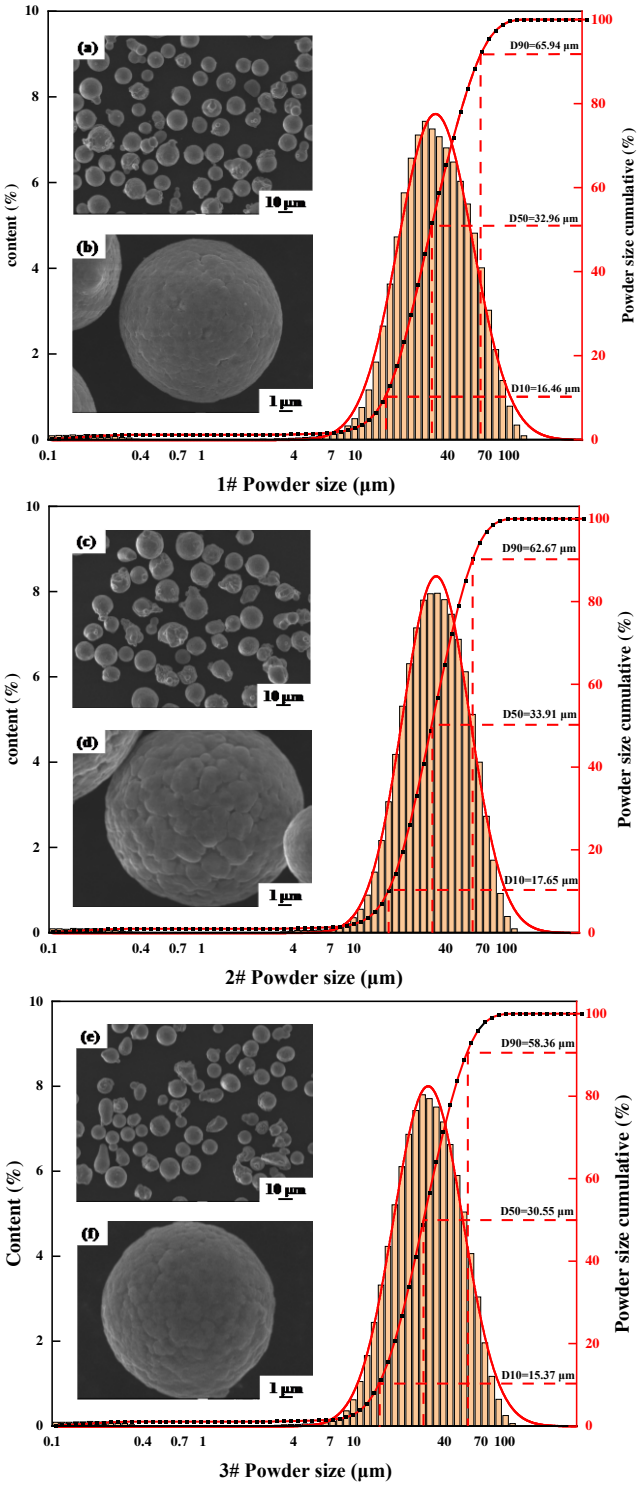

Figure 1. Powder morphology and particle size distribution(a) (b) 1# alloy powder morphology; (c) (d) 2# alloy powder morphology; (e) (f) 3# alloy powder morphology.

Table 1. The design composition of Al-Cu-Li-Mg-Ag-Sc-Zr powder.

Elements/wt.%	Cu	Li	Mg	Ag	Sc	Zr	Al
2195	3.7~4.3	0.8~1.2	0.25~0.8	0.25~0.6	/	0.08~0.16	Bal.
1#	4	1	0.8	0.5	0.8	0.4	Bal.
2#	4	2	0.8	0.5	0.8	0.4	Bal.
3#	4	3	0.8	0.5	0.8	0.4	Bal.

Preprints (www.preprints.org) | NOT PEER-REVIEWED | Posted: 29 December 2023 doi:10.20944/preprints202312.2226.v1

2.2. Forming Process

In this experiment, the EP-M250 metal 3D printing system (Beijing e Plus 3D Technology Co., Ltd.) was used, with a maximum laser power of 500 W and a spot diameter of 70 μm. Argon was used as the protective gas, and the oxygen content in the cavity of the 3D printing system was strictly controlled to be less than 100 ppm. The SLM process is accompanied by the interactions between the powder and the laser, and several process parameters affect the quality of the formed alloy, such as volumetric energy density (E), scanning speed (V), layer thickness (D), hatch spacing (H), laser power (P) and preheating temperature of the deposited substrate. Different process parameters also lead to large differences in the forming quality, surface morphology, microstructure, and mechanical properties of the alloys, so figuring out the optimal process parameters is the primary objective. Some of the above-mentioned process parameters have the following mathematical relationships as shown in Equation (1)[32]:

$$E = P/(V \times H \times D) \quad (1)$$

The preheating temperature of the deposition substrate was set at 140 degrees Celsius, and a parallel scanning strategy was used with 67° rotation per layer in the scanning direction, and a horizontal sample with dimensions of 65 mm × 11 mm × 11 mm was printed for subsequent experiments. The SLM process parameters were set as follows: P = 150 ~ 270 W, E = 80 ~ 240 J/mm, H = 0.1 mm, D = 0.03 mm. After a wide range of process parameters forming, the process parameters with the highest forming density are selected. The surface quality of the specimens under these processes was good, with no cracks. The chemical compositions of the powder and formed samples are shown in the Table 2. During the forming process, the Li loss rate is about 15%, the low melting point elements such as Li and Mg evaporate and blow away in the form of soot, resulting in a decrease in the content of Li and Mg in the formed sample. The theoretical density of alloys 1#, 2# and 3# was calculated from the chemical composition of the formed specimens as 2.64 g/cm^3, 2.51 g/cm^3 and 2.41 g/cm^3, respectively.

Table 2. Composition of raw powder and as-formed samples.

Elements/wt.%		Cu	Li	Mg	Ag	Sc	Zr	Al
Raw powder	1#	3.78	1.24	0.59	0.40	0.80	0.42	Bal.
	2#	3.92	2.67	0.67	0.53	0.76	0.42	Bal.
	3#	3.90	3.71	0.66	0.58	0.76	0.52	Bal.
As-formed sample	1#	4.08	1.16	0.50	0.38	0.76	0.41	Bal.
	2#	4.18	2.26	0.34	0.42	0.74	0.42	Bal.
	3#	4.07	3.24	0.50	0.48	0.72	0.52	Bal.

2.3. Experimental Procedures

Vickers microhardness tests were carried out using a HXD-1000TM microhardness tester at a pressure of 10 N. In order to reduce the error, each sample is measured 5 times. When the density of the formed sample is measured, the sample surface is polished with sandpaper first, and then polished with polishing cloth combined with polishing paste. The direct reading solid density meter (SJ-300G, Shanghai Shuju Instrument Technology Co., Ltd, Shanghai, China) is used. Its working principle is Archimedean drainage principle. The densification of the prepared sample is calculated by calculating the ratio of the measured value to the theoretical density. Combined with X-ray computed Tomography (CT), V |tome| x s 240/180, GE Sensing & Inspection Technologies GmbH, Frankfurt, Germany, the defects in the entire sample volume can be highlighted, and the density measured by the drainage method can also be verified.

The porosity defects and melt pool morphology inside the formed specimens were observed by Axiovert 200 MAT optical microscope (OM) after corrosion with Kaller's reagent for 10~15s. The phase analysis was carried out using an X'Pert Pro MPD analyzer from Panalytical, The Netherlands, with a step size of 0.033° per scan. The microstructure and morphology of the SLM formed parts were

Preprints (www.preprints.org) | NOT PEER-REVIEWED | Posted: 29 December 2023 doi:10.20944/preprints202312.2226.v1

observed and analyzed by a JSM-7900F field emission scanning electron microscope (SEM), and the molten pool morphology, grain size, and the second phase of the alloy were analyzed by an energy spectrum instrument (EDS), electron channel diffraction (ECC), and backscattering diffraction, which were equipped with the equipment. To observe and analyze the grains and the second phase on the micron and even nanometer scale, an FEI G2 60-300 and an FEI Tecnai F20 Transmission Electron Microscope (TEM) and the accompanying energy dispersive spectrometers (EDS) were used. Room temperature tensile tests were performed on an Instron-3382 electronic universal material testing machine, and the test procedure was performed in accordance with the test standard GB / T228.1 - 2010. The shape and dimensions of the tensile specimens are shown in the Figure 2.

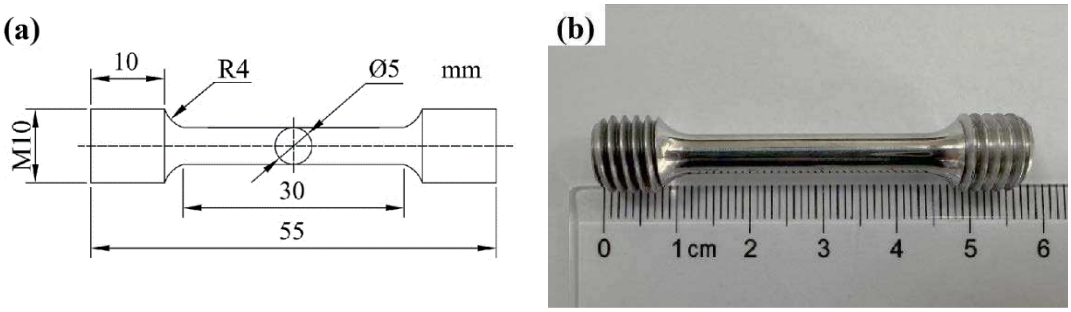

Figure 2. (a) Schematic diagram of a tensile bar specimen; (b) real sample.

3. Results and Discussion

3.1. Forming Process Optimization

The optimization of the SLM forming process for different materials is an essential step toward the fabrication of components with good performance. The laser power is 150 W, 180 W, 210 W, 240 W, 270 W, and the energy density is 80 J/mm^3, 90 J/mm^3, 120 J/mm^3, 150 J/mm^3, 180 J/mm^3, 210 J/mm^3, 240 J/mm^3 for a wide range of process optimization, the scanning spacing of 0.1 mm and layer thickness of 0.03 mm were used. Specimen densification is an important indicator of the quality of forming. Figure 3, 4 and 5 show the relationship between energy density and sample densification at the same laser power. The densification of the alloys formed by SLM decreased as the Li content increased, the highest densification of 99.58%, 99.12% and 93.03% can be obtained respectively, under the optimal process. The optimized SLM forming processes for these alloys were as follows: 1# alloy (P = 150 W, V = 556 mm/s, E = 90 J/mm^3), 2# alloy (P = 150 W, V = 417 mm/s, E = 120 J/mm^3) and 3# alloy (P = 150 W, V = 278 mm/s, E = 180 J/mm^3). The specimens' surface quality was good with no cracks. As the laser power or energy density increases, the overall trend of densification decreases, and the SLM forming process is sensitive to the Li content, which leads to a narrow forming process window. High energy density corresponds to low scanning speed, slow cooling speed, and long residence time at high temperatures inside the molten pool, which aggravates the volatilization of low melting point elements of Li and Mg, thus forming round pores and decreasing the densification of the formed specimens. High laser power will lead to high temperature of the melt pool, and the impact of the laser beam on the melt pool becomes strong, resulting in a large number of melt pool splash droplets. These splash droplets will lead to spherical bumps on the surface, slagging and other phenomena.

Preprints (www.preprints.org) | NOT PEER-REVIEWED | Posted: 29 December 2023 doi:10.20944/preprints202312.2226.v1

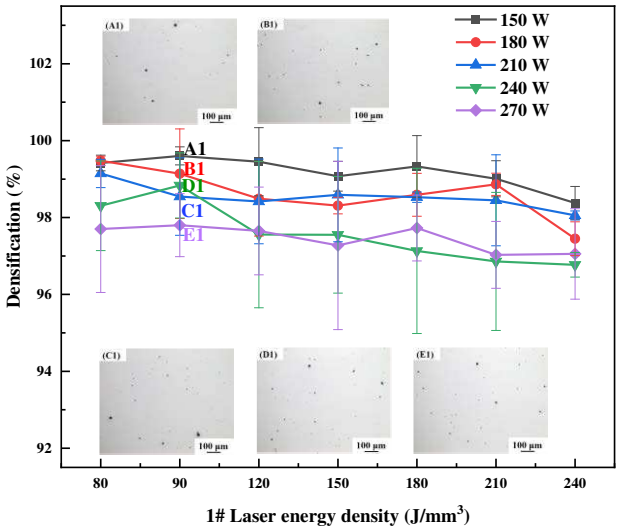

Figure 3. Densification of SLM formed 1# alloy at different process parameters.

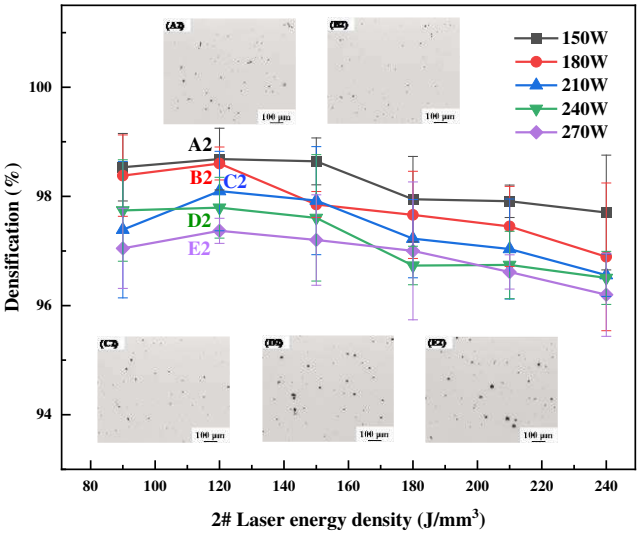

Figure 4. Densification of SLM formed 2# alloy at different process parameters.

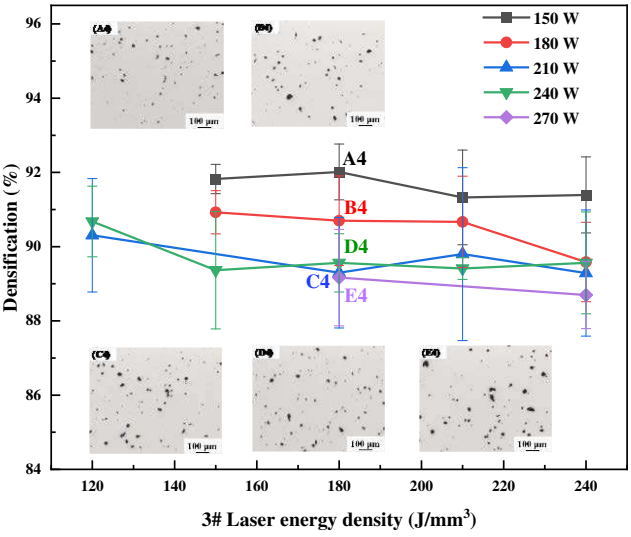

Preprints (www.preprints.org) | NOT PEER-REVIEWED | Posted: 29 December 2023 doi:10.20944/preprints202312.2226.v1

Figure 5. Densification of SLM formed 3# alloy at different process parameters.

The highest densification measured by the drainage method was confirmed by industrial CT, and the results are presented in Figure 6. The results show that the densification of alloy 1#, 2# and 3# are 99.51%, 98.96% and 92.01%, respectively. The final density was determined by industrial CT. Most of the pores in the sample are spherical, which accords with the characteristics of volatile pores, and a few irregular pores are presumed to be some incomplete melting powder gaps. The rounder the pore shape, the more uniform the stress distribution, the higher the Young's modulus and ultimate tensile strength of the material.

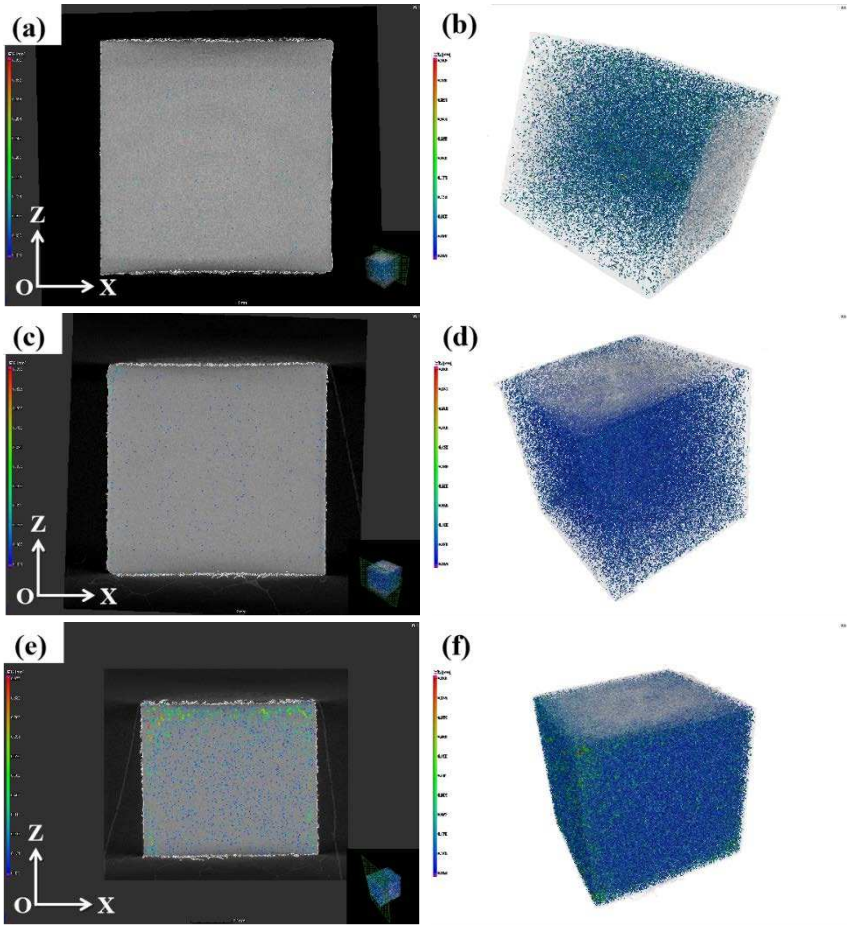

Figure 6. The microscopic defect distribution of XOZ cross section and the whole sample of SLM formed alloy: (a) (b) 1#; (c) (d) 2#; (e) (f) 3#.

3.2. Microstructure and Phase Analysis

3.2.1. Microstructure

Figure 7 shows the backscattered electron (BSE) SEM photographs of the samples. The white dashed lines are labeled as melt pool boundaries (MPBs). The solidification temperature range (STR) during the SLM process is prolonged due to the presence of Li element. The SLM solidification process is found to depend on the cooling rate, where a fast-cooling rate leads to coarse columnar grains with a <100>crystal orientation (perpendicular to the MPBs). Columnar epitaxial growth nucleating on the dendritic substrate occurs throughout the SLM-processed cubic samples. It is worth noting that the large STR also enhances the crack sensitivity during SLM. Large number of white precipitates are visible near grain boundaries (GBs), MPBs, and intracrystalline. Due to the high cooling rate of 10^5 - 10^7 / s in SLM, the precipitated phases are dispersed.

Preprints (www.preprints.org) | NOT PEER-REVIEWED | Posted: 29 December 2023 doi:10.20944/preprints202312.2226.v1

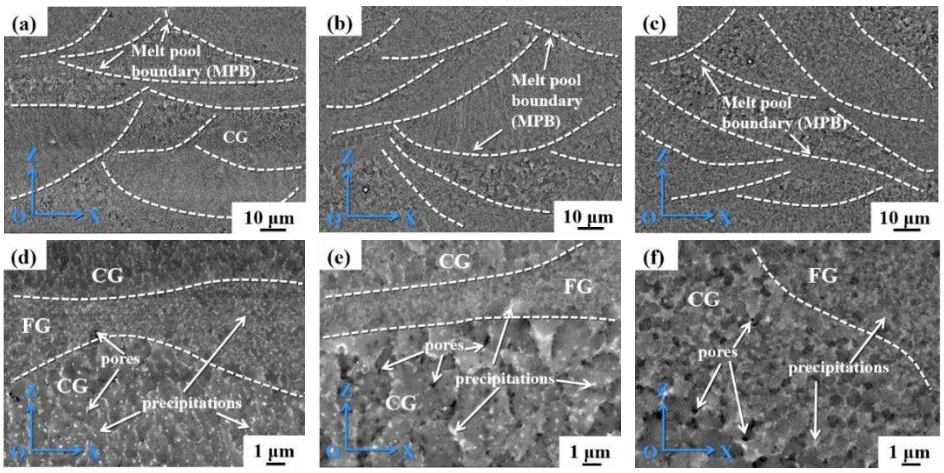

Figure 7. SEM morphology of the SLM formed Al-Li alloy: (a) (d) 1#; (b) (e) 2#; (c) (f) 3#.

As can be seen from the EBSD morphology in Figure 8, 9 and 10, the SLM formed 1#, 2# and 3# alloys have typical heterogeneous structures, i.e., alternating columnar grains (CG) and fine equiaxed grains (FG). The SLM specimens show a bimodal grain structure consisting of fine equiaxial grains and fine columnar grains. The equiaxial grains are mainly distributed at the melt pool boundary and the columnar grains are mainly distributed inside the melt pool. Similar microstructures were observed in other Sc and Zr modified aluminum alloys prepared by SLM[33–35]. The equiaxed regions are due to the large number density of incipient Al_3(Sc, Zr) nucleation sites. The columnar region is associated with a low density of nucleation sites associated with high-temperature gradients. The average grain sizes of SLM formed alloys are 2.6 μm, 2.1 μm and 1.8 μm, respectively. The laser scanning speed of the three alloys gradually slows down, but the grain size is smaller. The reason is that the increase of lithium content is helpful to form more strengthening phases containing Li incoherent structure, such as T_1 and T_2 phase, which can form strengthening regions near grain boundaries and promote the formation of FG.

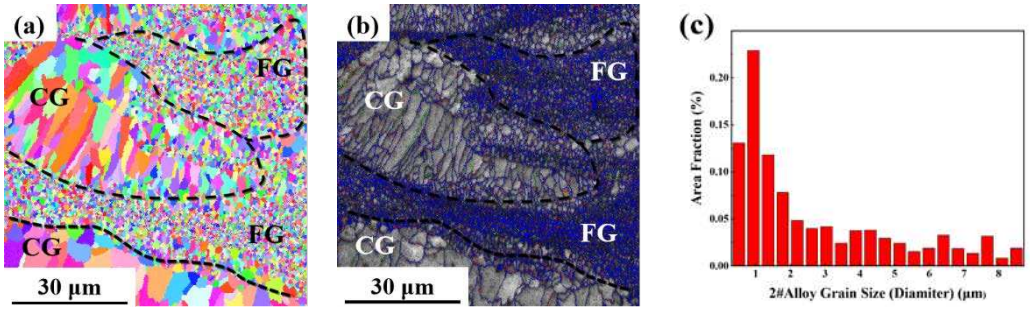

Figure 8. EBSD analysis result of SLM formed 1# Al-Li alloy: (a) grain remodeling; (b) grain boundary remodeling; (c) grain size statistics.

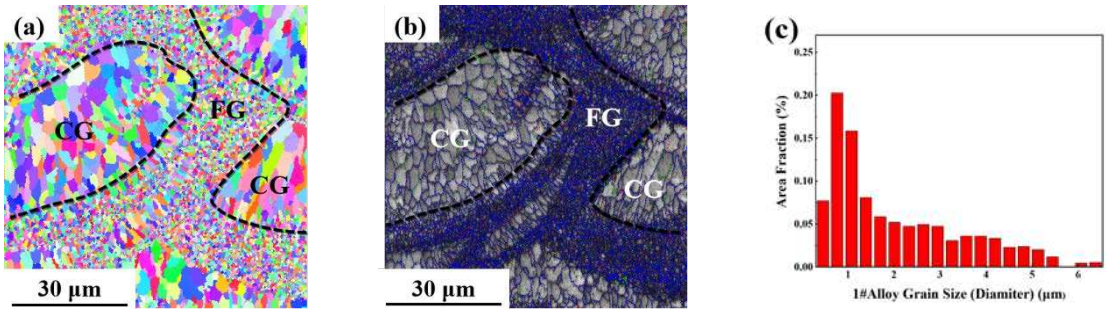

Figure 9. EBSD analysis result of SLM formed 2# Al-Li alloy: (a) grain remodeling; (b) grain boundary remodeling; (c) grain size statistics.

Preprints (www.preprints.org) | NOT PEER-REVIEWED | Posted: 29 December 2023 doi:10.20944/preprints202312.2226.v1

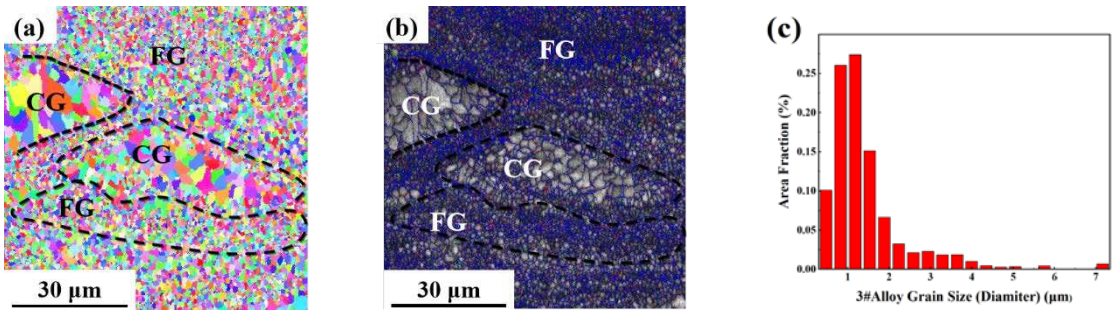

Figure 10. EBSD analysis result of SLM formed 3# Al-Li alloy: (a) grain remodeling; (b) grain boundary remodeling; (c) grain size statistics.

3.2.2. XRD Phase Analysis

Figure 11 shows the X-ray diffraction (XRD) patterns of the three as-formed alloys. The X-ray diffraction analysis demonstrated the existence of many phases inside the aluminum (α-Al) matrix, including θ (Al_2Cu), T_1 (Al_2CuLi), T_2 (Al_6CuLi_3) and T_B (Al_7CuLi_4). All three alloys' X-ray diffraction spectra displayed distinct and notable α-Al peaks. Diffraction peaks corresponding to Al_3(Sc, Zr) were not illustrated in the SLM formed Al-Li alloy. During SLM forming, the solid solubility of Sc, Zr increases obviously. This result is further influenced by the alloys' low concentrations of the elements Sc, Zr as well as the X-ray diffraction testing's limited sensitivity.

The variability in Li content is the primary factor that significantly affects the formation of Cu-containing phases. The precipitation of the θ (Al_2Cu) phase, T_1 (Al_2CuLi) phase and T_B (Al_7CuLi_4) phase is favored from both the α-Al phase and the liquid phase when the Li content is 1.0 wt.%. Upon further increasing the lithium content to about 2.0 wt.%, the T_1 phase is precipitated in conjunction with the T_2 (Al_6CuLi_3) phase. When the Li content reaches 3wt.%, the T_1 phase no longer precipitates, and the δ′ (Al_3Li) phase precipitates with the T_2 phase. The precipitation process can be briefly outlined as follows: θ → T_B → T_1 → T_2 → T_2 + δ′.

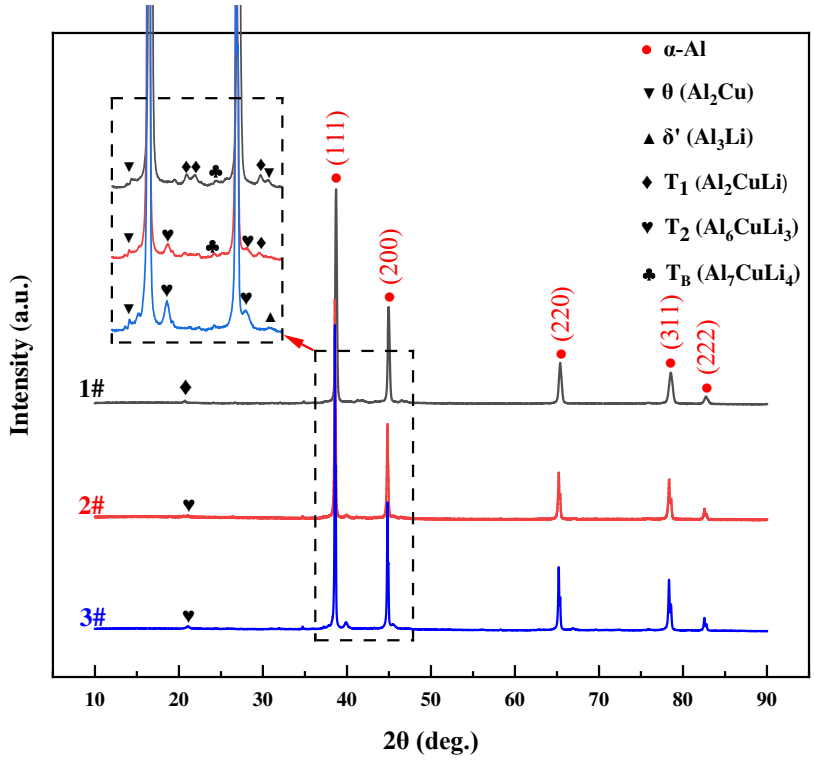

Figure 11. XRD patterns of SLM formed Al-Li alloy specimens.

Preprints (www.preprints.org) | NOT PEER-REVIEWED | Posted: 29 December 2023 doi:10.20944/preprints202312.2226.v1

3.3. TEM Morphology and Analysis

Figure 12 shows the microstructure of the interface between equiaxed grains and columnar grains in the molten pool of the as-printed alloy, TEM photos and diffraction analysis and TEM high-resolution photos. From the bright-field image of Figure 12a, d and g it can be seen that the size of the equiaxial grains is in the range of 0.5~1 μm, and the length of the columnar grains is in the range of about 2~5 μm. There are continuous strips of precipitates at the junction of the grains, many nanoscale particles are found within the grains of the columnar grains and equiaxial grains, which may be the precipitated phases such as θ (Al_2Cu) phase and primary Al_3(Sc, Zr) etc. In Figure 12b, e and h the SAED patterns of three Al-Li alloys are indexed to show the relative orientation relationships (ORs). From the HRSTEM image of Figure 12c, f and i the interface between the precipitated phase and the Al matrix can be seen. There is a certain dislocation between the precipitated phase and the atoms neighbor to the aluminum matrix. The dislocation cuts through the particles, the particles produce a new surface area, which increases the total interface energy, the atoms in the particles are staggered, which brings difficulties to the movement of dislocations and plays a strengthening effect.

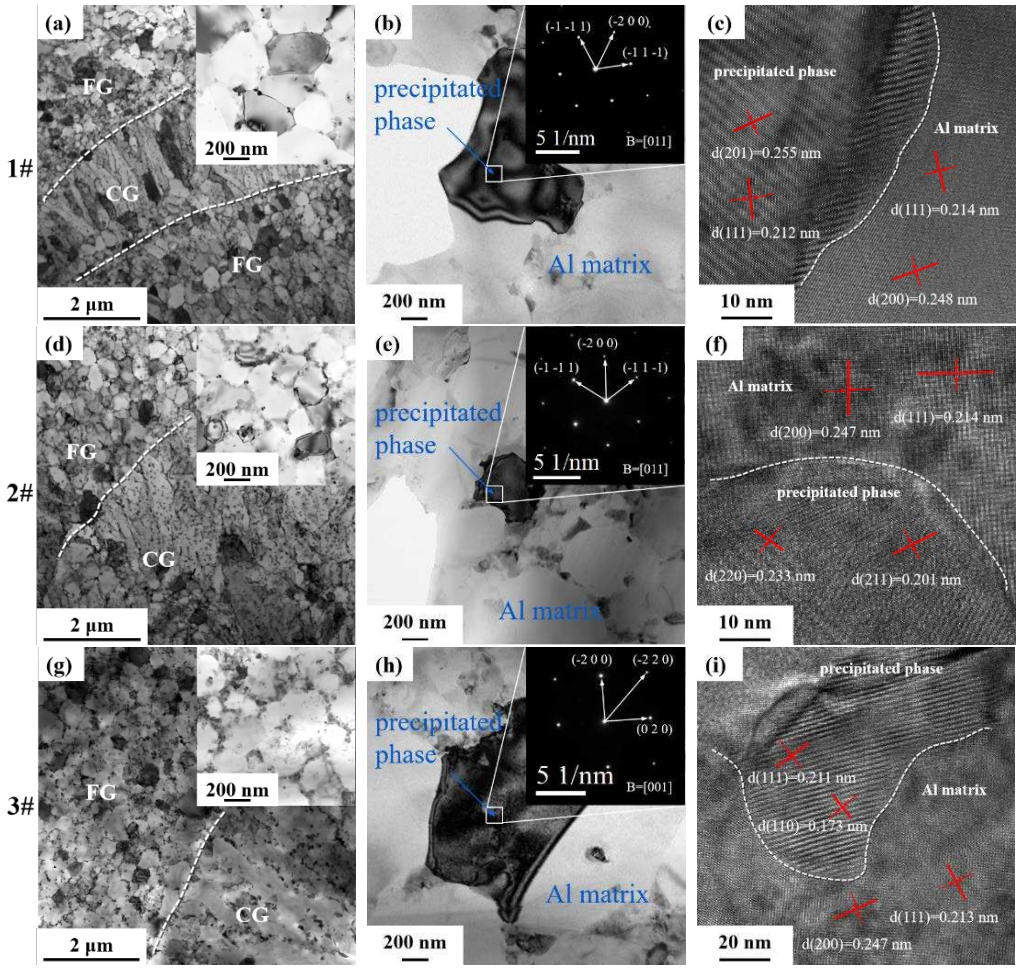

Figure 12. The morphological characteristics of equiaxed and columnar crystals of SLM-formed alloys under STEM: bright field (a) (d) (g); SAED pattern index and relative orientation relationship (ORs) (b) (e) (h); HRSTEM image of the interface between the precipitated phase and the Al matrix (c) (f) (i).

Figure 13a, b and c shows the distribution of Al, Cu, Mg, Ag, Sc, and Zr elements in 1 # 2 # and 3 # alloys determined by high-angle annular dark field (HAADF) images. It is well known that the elemental distribution of lithium cannot be directly detected by EDS or WDS. The distribution of Li-containing precipitates can be studied and speculated according to the distribution of other elements by EDS surface scanning. Most of the Cu and Sc elemental elements are precipitated at the grain

Preprints (www.preprints.org) | NOT PEER-REVIEWED | Posted: 29 December 2023 doi:10.20944/preprints202312.2226.v1

boundaries and cover part of the grain boundaries. The distribution of the Mg, Ag, and Zr elements is more uniform. The cooling rate at the bottom of the molten pool is lower than that inside the molten pool. The remelting at the bottom of the molten pool and the low overheating and slightly lower cooling rate led to the precipitation of primary Al_3(Sc, Zr) at the bottom, and these primary Al_3(Sc, Zr) can be used as nucleation centers to form equiaxed grains[36–39]. Columnar grains grow from the outer edges of the equiaxed grains and may introduce some incipient Al_3(Sc, Zr)[22,40].

The intensity of the images in HAADF is positively correlated with the atomic mass, and the analysis shows the presence of precipitates with different contrasts (white, gray, and black) in a single medium. Combined with the EDS results, the white precipitates are rich in Cu. These white precipitates are elliptical or small flakes, mostly located at grain boundaries, and are presumed to be T_1 or T_B phases containing Li elements.

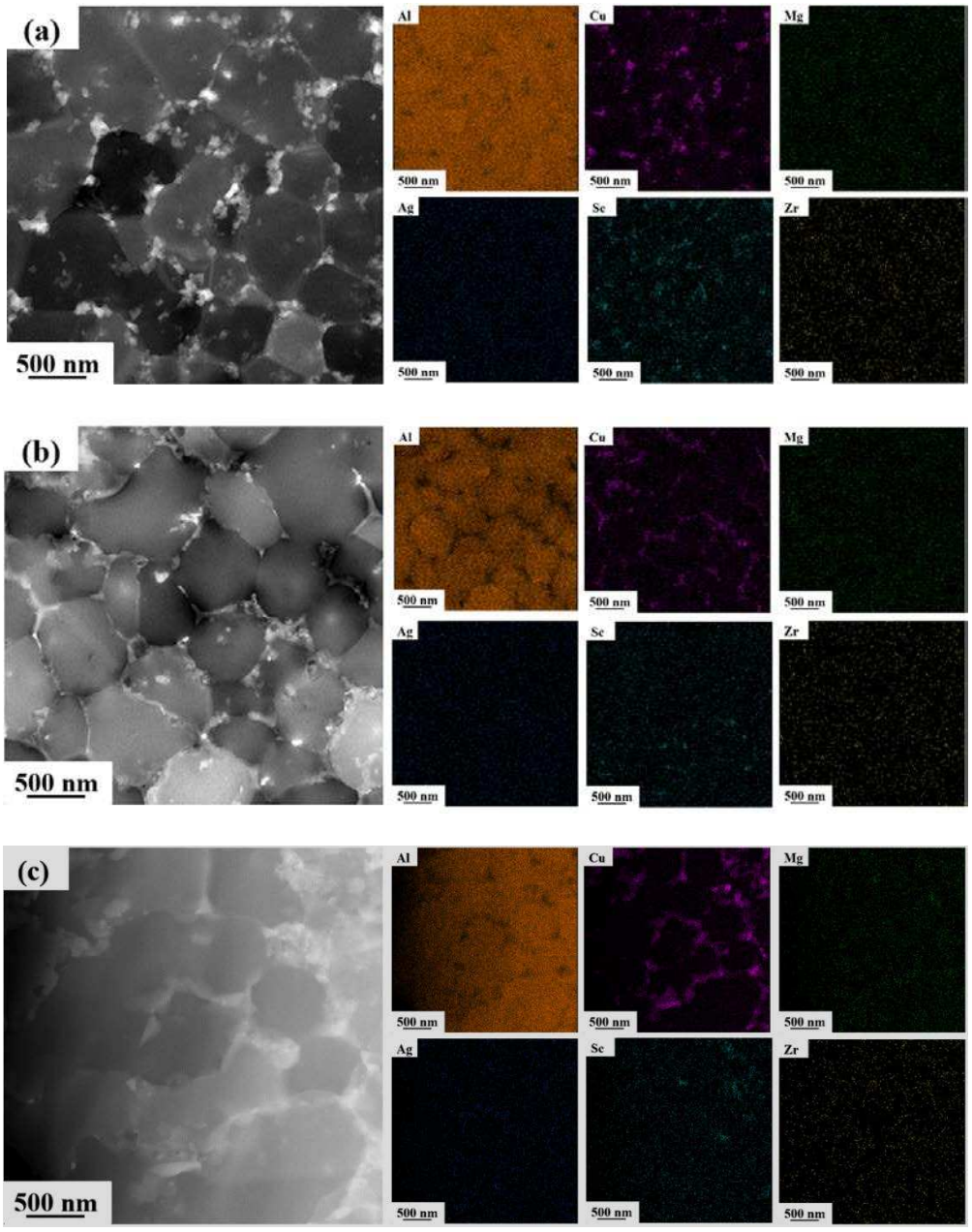

Figure 13. STEM HAADF images of SLM formed samples corresponding EDX mapping of the solute elements (Al, Cu, Mg, Ag, Sc, Zr) (a) 1 #; (b) 2 #; (c) 3 #.

Preprints (www.preprints.org) | NOT PEER-REVIEWED | Posted: 29 December 2023 doi:10.20944/preprints202312.2226.v1

3.4. Mechanical Propertie

The microhardness of the sample with the highest density was measured, the hardness values of 1 #, 2 # and 3 # alloys are 135 HV, 160 HV and 148 HV, respectively. With the increase of Li content, the microhardness of the alloy increases first and then decreases. The reason for the increase of hardness is that when the Li content increases to 2 wt.%, the T_1 strengthening phase of the formed alloy increases. The reason for the decrease in hardness is that when the Li content increases to 3 wt.%, the internal porosity of the alloy increases significantly.

The mechanical properties of the as-printed state of the three compositions are shown in the following Table 3 and Figure 14. The tensile properties of the as-printed state of the three compositions are close to those of the SLM formed 2195 alloy and commercial 2195 plate-T6[25,41], which requires an aging time of up to 180 h. The SLM process allows Al-Li alloys to utilize the elements Sc and Zr well beyond equilibrium solid solubility, with enhanced grain boundary strengthening from grain refinement. The rest of the good tensile properties might be ascribed to the solid solution strengthening of Sc, Zr and a little more Li in the Al matrix. Al-Li alloys are usually strengthened with the T_1 phase (Al_2CuLi) due to its highest strength, which generally precipitates during artificial aging and is rare in as formed samples. Therefore, the difference in Li content may affect the properties after heat treatment.

Table 3. The tensile properties of SLM formed as-printed 1 #, 2 #, 3 # alloys were compared with SLM formed 2195 alloy and 2195 plate after T6 heat treatment.

Samples	UTS（MPa）	YS（MPa）	Elongation（%）	Modulus（GPa）
1# AP	461.1 ± 11.7	412.6 ± 16.0	13.6 ± 1.1	73.3 ± 1.5
2# AP	514.8 ± 27.5	481.2 ± 37.9	4.9 ± 2.6	76.2 ± 2.5
3# AP	494.8 ± 16.5	477.5 ± 0.7	1 ± 0.7	74.2 ± 0.6
2195 T6[25]	587.0 ± 7.5	512.3 ± 14.4	6.9 ± 0.3	/
2195 plate-T6[41]	560.0 ± 4.2	497.0 ± 1.9	6.8 ± 0.4	/

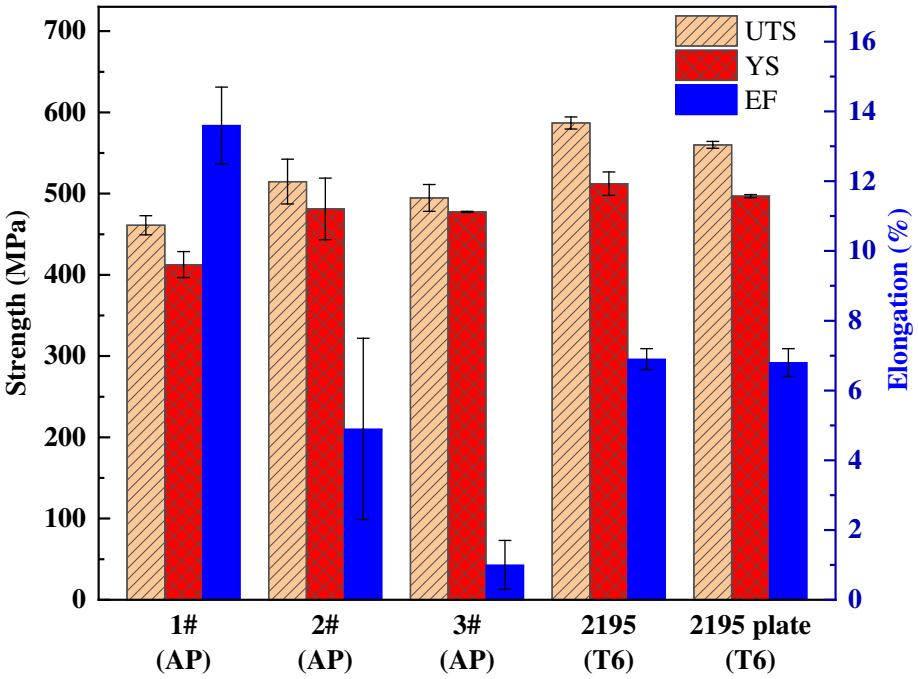

Figure 14. The tensile properties of SLM formed as-printed 1 #, 2 #, 3 # alloys and SLM formed 2195 alloy and 2195 plate after T6 heat treatment were compared with the histogram.

Preprints (www.preprints.org) | NOT PEER-REVIEWED | Posted: 29 December 2023 doi:10.20944/preprints202312.2226.v1

4. Conclusions

In this paper, the SLM forming of Al-Cu-Li-Mg-Ag-Sc-Zr alloys with different Li contents is studied. The differences in porosity, microstructure, and mechanical properties of the as-formed specimens of the three alloys are compared. The main conclusions are as follows:

1. The alloys with different Li contents successfully prepared by SLM technology are crack-free, with good surface quality and high densification of 99.51%, 98.96% and 92.01% respectively.
2. With the increase of laser power and energy density, the overall trend of densification decreases gradually, and the process window of forming is narrowed by the increase of Li content, and the SLM forming process is very sensitive to Li content. At high energy density, the cooling speed of the melt pool is slow, and the internal high temperature residence time is long, which aggravates the volatilization of the low melting point elements Li and Mg, thus forming round pores and decreasing the densification of the formed specimens.
3. When the Li content is 1.0 wt.%, there are θ phase, T_1 phase and T_B phase, and when the Li content is increased to about 2.0 wt.%, the T_1 and T_2 phases are precipitated together; when the Li content is 3.0 wt.%, the δ′ phase precipitates together with the T_2 phase.
4. With the increase of Li content, the hardness, tensile strength, yield strength and modulus of elasticity of 1#, 2# and 3# alloys firstly increase and then decrease, and the elongation after break, section shrinkage decrease. There are two possible reasons for the analysis: First, with the gradual increase of Li content, the pore defects in the formed samples become more and more; Second, when the content of Li element increases to 3wt.%, the main reinforcing phase T_1 phase no longer precipitates.

The Li content in the existing Al-Li alloys is less than 2.5 wt.%, but the maximum solubility of Li in the α-Al phase is 4.2 wt.%. The slow cooling rate during casting will form brittle phase δ-AlLi phase, which is unfavorable to mechanical properties and corrosion resistance. In contrast, the cooling rate of SLM is very fast, and the Li is uniformly distributed in the α-Al phase, avoiding the formation of the δ phase, so that Al-Li alloys with high Li content can be SLM formed. Through the optimization of process parameter adjustment and microalloying grain refinement by adding Sc and Zr to form Al_3(Sc, Zr) particles in the alloy as a non-uniform nucleating agent, the crack control is achieved and the window of SLM process is widened. The rapid manufacturing and development of new aluminum-lithium alloy structural parts at relatively low cost through the SLM process can meet the development of the aerospace field, which has important prospects for development and application.

Author Contributions: S.S.: Conceptualization, Investigation, Data Curation, Validation, Writing-Original Draft, Writing-Review & Editing. Z.L.: Visualization, Writing-Review & Editing. P.Y.: Conceptualization, Resources, Validation. X.L.: Conceptualization, Resources, Supervision. Y.Z.: Conceptualization, Resources, Writing-Review & Editing.

Funding: This research received no external funding.

Institutional Review Board Statement: Not applicable.

Informed Consent Statement: Not applicable.

Data Availability Statement: Date are contained within the article.

Acknowledgments: The financial support by GRINM Metal Composites Technology Co., Ltd. And research platform support by National Engineering & Technology Research Center for Non-ferrous Metal Matrix Composites, GRINM Group Co., Ltd. are greatly acknowledged.

Conflicts of Interest: The authors declare no conflict of interest.

Preprints (www.preprints.org) | NOT PEER-REVIEWED | Posted: 29 December 2023 doi:10.20944/preprints202312.2226.v1

References

1. Li, S.S.; Yue, X.; Li, Q.Y.; Peng, H.L.; Dong, B.X.; Liu, T.S.; Yang, H.Y.; Fan, J.; Shu, S.L.; Qiu, F.; Jiang, Q.C., Development and applications of aluminum alloys for aerospace industry. *J. Mater. Res. Technol.* **2023**, 27, 944-983. https://doi.org/10.1016/j.jmrt.2023.09.274
2. Kablov, E.N.; Antipov, V.V.; Oglodkova, J.S.; Oglodkov, M.S., Development and Application Prospects of Aluminum–Lithium Alloys in Aircraft and Space Technology. *Metallurgist*. **2021**, 65, 72-81. https://doi.org/10.1007/s11015-021-01134-9
3. Xu, R.; Li, R.; Yuan, T.; Niu, P.; Wang, M.; Lin, Z., Microstructure, metallurgical defects and hardness of Al–Cu–Mg–Li–Zr alloy additively manufactured by selective laser melting. *J. Alloys Compd.* **2020**, 835, 155372. https://doi.org/10.1016/j.jallcom.2020.155372
4. Raffeis, I.; Adjei-Kyeremeh, F.; Vroomen, U.; Richter, S.; Buhrig-Polaczek, A., Characterising the Microstructure of an Additively Built Al-Cu-Li Alloy. *Materials.* **2020**, 13, 5188. https://doi.org/10.3390/ma13225188
5. Sun, Z.; Wang, H.; Tian, X.; He, B., Developing a novel lightweight Al–Mg–Li alloy for laser powder bed fusion additive manufacturing: Parameter optimization, microstructure evolution, and mechanical performance. *Mater. Sci. Eng., A*. **2023**, 872, 144992. https://doi.org/10.1016/j.msea.2023.144992
6. Kempen, K.; Thijs, L.; Van Humbeeck, J.; Kruth, J.P., Mechanical Properties of AlSi10Mg Produced by Selective Laser Melting. *Phys. Procedia*. **2012**, 39, 439-446. https://doi.org/10.1016/j.phpro.2012.10.059
7. Brandl, E.; Heckenberger, U.; Holzinger, V.; Buchbinder, D., Additive manufactured AlSi10Mg samples using Selective Laser Melting (SLM): Microstructure, high cycle fatigue, and fracture behavior. *Mater. Des.* **2012**, 34, 159-169. https://doi.org/10.1016/j.matdes.2011.07.067
8. Zhang, H.; Zhu, H.; Qi, T.; Hu, Z.; Zeng, X., Selective laser melting of high strength Al–Cu–Mg alloys: Processing, microstructure and mechanical properties. *Mater. Sci. Eng., A*. **2016**, 656, 47-54. https://doi.org/10.1016/j.msea.2015.12.101
9. Martin, J.H.; Yahata, B.D.; Hundley, J.M.; Mayer, J.A.; Schaedler, T.A.; Pollock, T.M., 3D printing of high-strength aluminium alloys. *Nature*. **2017**, 549, 365-369. https://doi.org/10.1038/nature23894
10. Qi, T.; Zhu, H.; Zhang, H.; Yin, J.; Ke, L.; Zeng, X., Selective laser melting of Al7050 powder: Melting mode transition and comparison of the characteristics between the keyhole and conduction mode. *Mater. Des.* **2017**, 135, 257-266. https://doi.org/10.1016/j.matdes.2017.09.014
11. Nie, X.; Chen, Z.; Qi, Y.; Zhang, H.; Zhang, C.; Xiao, Z.; Zhu, H., Effect of defocusing distance on laser powder bed fusion of high strength Al–Cu–Mg–Mn alloy. *Virtual Phys. Prototyp.* **2020**, 15, 325-339. https://doi.org/10.1080/17452759.2020.1760895
12. Schmidtke, K.; Palm, F.; Hawkins, A.; Emmelmann, C., Process and Mechanical Properties: Applicability of a Scandium modified Al-alloy for Laser Additive Manufacturing. *Phys. Procedia*. **2011**, 12, 369-374. https://doi.org/10.1016/j.phpro.2011.03.047
13. Spierings, A.B.; Dawson, K.; Heeling, T.; Uggowitzer, P.J.; Schäublin, R.; Palm, F.; Wegener, K., Microstructural features of Sc- and Zr-modified Al-Mg alloys processed by selective laser melting. *Mater. Des.* **2017**, 115, 52-63. https://doi.org/10.1016/j.matdes.2016.11.040
14. Spierings, A.B.; Dawson, K.; Kern, K.; Palm, F.; Wegener, K., SLM-processed Sc- and Zr- modified Al-Mg alloy: Mechanical properties and microstructural effects of heat treatment. *Mater. Sci. Eng., A*. **2017**, 701, 264-273. https://doi.org/10.1016/j.msea.2017.06.089
15. Wang, Y.; Liu, H.; Ma, X.; Wu, R.; Sun, J.; Hou, L.; Zhang, J.; Li, X.; Zhang, M., Effects of Sc and Zr on microstructure and properties of 1420 aluminum alloy. *Mater. Charact.* **2019**, 154, 241-247. https://doi.org/10.1016/j.matchar.2019.06.001
16. Samuel, A.M.; Alkahtani, S.A.; Doty, H.W.; Samuel, F.H., Role of Zr and Sc addition in controlling the microstructure and tensile properties of aluminum–copper based alloys. *Mater. Des.* **2015**, 88, 1134-1144. https://doi.org/10.1016/j.matdes.2015.09.090
17. Muhammad, A.; Xu, C.; Xuejiao, W.; Hanada, S.; Yamagata, H.; Hao, L.; Chaoli, M., High strength aluminum cast alloy: A Sc modification of a standard Al–Si–Mg cast alloy. *Mater. Sci. Eng., A*. **2014**, 604, 122-126. https://doi.org/10.1016/j.msea.2014.03.005
18. Taendl, J.; Orthacker, A.; Amenitsch, H.; Kothleitner, G.; Poletti, C., Influence of the degree of scandium supersaturation on the precipitation kinetics of rapidly solidified Al-Mg-Sc-Zr alloys. *Acta Mater.* **2016**, 117, 43-50. https://doi.org/10.1016/j.actamat.2016.07.001
19. Nie, X.; Zhang, H.; Zhu, H.; Hu, Z.; Ke, L.; Zeng, X., Effect of Zr content on formability, microstructure and mechanical properties of selective laser melted Zr modified Al-4.24Cu-1.97Mg-0.56Mn alloys. *J. Alloys Compd.* **2018**, 764, 977-986. https://doi.org/10.1016/j.jallcom.2018.06.032

Preprints (www.preprints.org) | NOT PEER-REVIEWED | Posted: 29 December 2023 doi:10.20944/preprints202312.2226.v1

20. Zhang, H.; Zhu, H.; Nie, X.; Yin, J.; Hu, Z.; Zeng, X., Effect of Zirconium addition on crack, microstructure and mechanical behavior of selective laser melted Al-Cu-Mg alloy. *Scr. Mater.* **2017**, 134, 6-10. https://doi.org/10.1016/j.scriptamat.2017.02.036
21. Lu, Y.; Zhang, H.; Xue, P.; Wu, L.; Liu, F.; Jia, L.; Ni, D.; Xiao, B.; Ma, Z., Microstructural Evaluation and Tensile Properties of Al-Mg-Sc-Zr Alloys Prepared by LPBF. *Crystals*. **2023**, 13, 913. https://doi.org/10.3390/cryst13060913
22. Pan, W.; Zhai, Z.; Liu, Y.; Liang, B.; Liang, Z.; Zhang, Y., Research on Microstructure and Cracking Behavior of Al-6.2Zn-2Mg-xSc-xZr Alloy Fabricated by Selective Laser Melting. *Crystals*. **2022**, 12, 1500. https://doi.org/10.3390/cryst12101500
23. Liu, D.; Yürekli, B.; Ullsperger, T.; Matthäus, G.; Schade, L.; Nolte, S.; Rettenmayr, M., Microstructural aspects of additive manufacturing of Al Li alloys with high Li content. *Mater. Des.* **2021**, 198, 109323. https://doi.org/10.1016/j.matdes.2020.109323
24. Li, L.; Meng, X.; Huang, S.; Wang, H.; Li, P.; Zhou, J., Investigating the effect of the scanning speed on the characteristics of Al-Li alloy fabricated by selective laser melting. *J. Manuf. Processes*. **2022**, 75, 719-728. https://doi.org/10.1016/j.jmapro.2022.01.040
25. Qi, Y.; Zhang, H.; Nie, X.; Hu, Z.; Zhu, H.; Zeng, X., A high strength Al–Li alloy produced by laser powder bed fusion: Densification, microstructure, and mechanical properties. *Addit. Manuf.* **2020**, 35, 101346. https://doi.org/10.1016/j.addma.2020.101346
26. Qi, Y.; Hu, Z.; Zhang, H.; Nie, X.; Zhang, C.; Zhu, H., High strength Al–Li alloy development for laser powder bed fusion. *Addit. Manuf.* **2021**, 47, 102249. https://doi.org/10.1016/j.addma.2021.102249
27. Sun, Z.; He, B.; Li, K.; Tu, Y.; Wang, H., Study on microstructure evolution and aging precipitation behavior of a novel Al-Li alloy fabricated by laser rapid melting. *J. Alloys Compd.* **2022**, 908, 164630. https://doi.org/10.1016/j.jallcom.2022.164630
28. Yürekli, B.; Schade, L.; Ullsperger, T.; Seyfarth, B.; Kohl, H.; Matthäus, G.; Liu, D.; Rettenmayr, M.; Nolte, S., Additive manufacturing of binary Al-Li alloys. *Procedia CIRP*. **2020**, 94, 69-73. https://doi.org/10.1016/j.procir.2020.09.014
29. Wang, A.; Yan, Y.; Chen, Z.; Qi, H.; Yin, Y.; Wu, X.; Jia, Q., Characterisation of the multiple effects of Sc/Zr elements in selective laser melted Al alloy. *Mater. Charact.* **2022**, 183, 111653. https://doi.org/10.1016/j.matchar.2021.111653
30. Zhai, Z.; Pan, W.; Liang, B.; Liu, Y.; Zhang, Y., Cracking Behavior, Microstructure and Properties of Selective Laser Melted Al-Mn-Mg-Sc-Zr Alloy. *Crystals*. **2022**, 12, 565. https://doi.org/10.3390/cryst12040565
31. Yin, P.; Liu, Y.; Liang, Z.; Pan, W.; Shao, S.; Zhang, Y., Microstructure, Mechanical Properties and Fracture Behavior of Micron-Sized TiB(2)/AlZnMgCu(Sc,Zr) Composites Fabricated by Selective Laser Melting. *Materials*. **2023**, 16, 2112. https://doi.org/10.3390/ma16052112
32. Qu, M.; Guo, Q.; Escano, L.I.; Nabaa, A.; Hojjatzadeh, S.M.H.; Young, Z.A.; Chen, L., Controlling process instability for defect lean metal additive manufacturing. *Nat. Commun.* **2022**, 13, 1079. https://doi.org/10.1038/s41467-022-28649-2
33. Wang, P.; Deng, L.; Prashanth, K.G.; Pauly, S.; Eckert, J.; Scudino, S., Microstructure and mechanical properties of Al-Cu alloys fabricated by selective laser melting of powder mixtures. *J. Alloys Compd.* **2018**, 735, 2263-2266. https://doi.org/10.1016/j.jallcom.2017.10.168
34. Wang, Z.; Lin, X.; Kang, N.; Hu, Y.; Chen, J.; Huang, W., Strength-ductility synergy of selective laser melted Al-Mg-Sc-Zr alloy with a heterogeneous grain structure. *Addit. Manuf.* **2020**, 34, 101260. https://doi.org/10.1016/j.addma.2020.101260
35. Wang, Z.; Lin, X.; Kang, N.; Wang, Y.; Yu, X.; Tan, H.; Yang, H.; Huang, W., Making selective-laser-melted high-strength Al–Mg–Sc–Zr alloy tough via ultrafine and heterogeneous microstructure. *Scr. Mater.* **2021**, 203, 114052. https://doi.org/10.1016/j.scriptamat.2021.114052
36. Spierings, A.B.; Dawson, K.; Voegtlin, M.; Palm, F.; Uggowitzer, P.J., Microstructure and mechanical properties of as-processed scandium-modified aluminium using selective laser melting. *CIRP Annals*. **2016**, 65, 213-216. https://doi.org/10.1016/j.cirp.2016.04.057
37. Kurz, W.; Bezençon, C.; Gäumann, M., Columnar to equiaxed transition in solidification processing. *Sci. Technol. Adv. Mater.* **2001**, 2, 185-191. https://doi.org/10.1016/s1468-6996(01)00047-x
38. Gäumann, M.; Henry, S.; Cléton, F.; Wagnière, J.D.; Kurz, W., Epitaxial laser metal forming: analysis of microstructure formation. *Mater. Sci. Eng., A*. **1999**, 271, 232-241. https://doi.org/10.1016/s0921-5093(99)00202-6
39. Kotadia, H.R.; Gibbons, G.; Das, A.; Howes, P.D., A review of Laser Powder Bed Fusion Additive Manufacturing of aluminium alloys: Microstructure and properties. *Addit. Manuf.* **2021**, 46, 102155. https://doi.org/10.1016/j.addma.2021.102155

Preprints (www.preprints.org) | NOT PEER-REVIEWED | Posted: 29 December 2023 doi:10.20944/preprints202312.2226.v1

40. Jia, Z.-h.; RØYset, J.; Solberg, J.K.; Liu, Q., Formation of precipitates and recrystallization resistance in Al–Sc–Zr alloys. *Trans. Nonferrous Met. Soc. China*. **2012**, 22, 1866-1871. https://doi.org/10.1016/s1003-6326(11)61399-x
41. Kim, J.-H.; Jeun, J.-H.; Chun, H.-J.; Lee, Y.R.; Yoo, J.-T.; Yoon, J.-H.; Lee, H.-S., Effect of precipitates on mechanical properties of AA2195. *J. Alloys Compd.* **2016**, 669, 187-198. https://doi.org/10.1016/j.jallcom.2016.01.229

Disclaimer/Publisher's Note: The statements, opinions and data contained in all publications are solely those of the individual author(s) and contributor(s) and not of MDPI and/or the editor(s). MDPI and/or the editor(s) disclaim responsibility for any injury to people or property resulting from any ideas, methods, instructions or products referred to in the content.